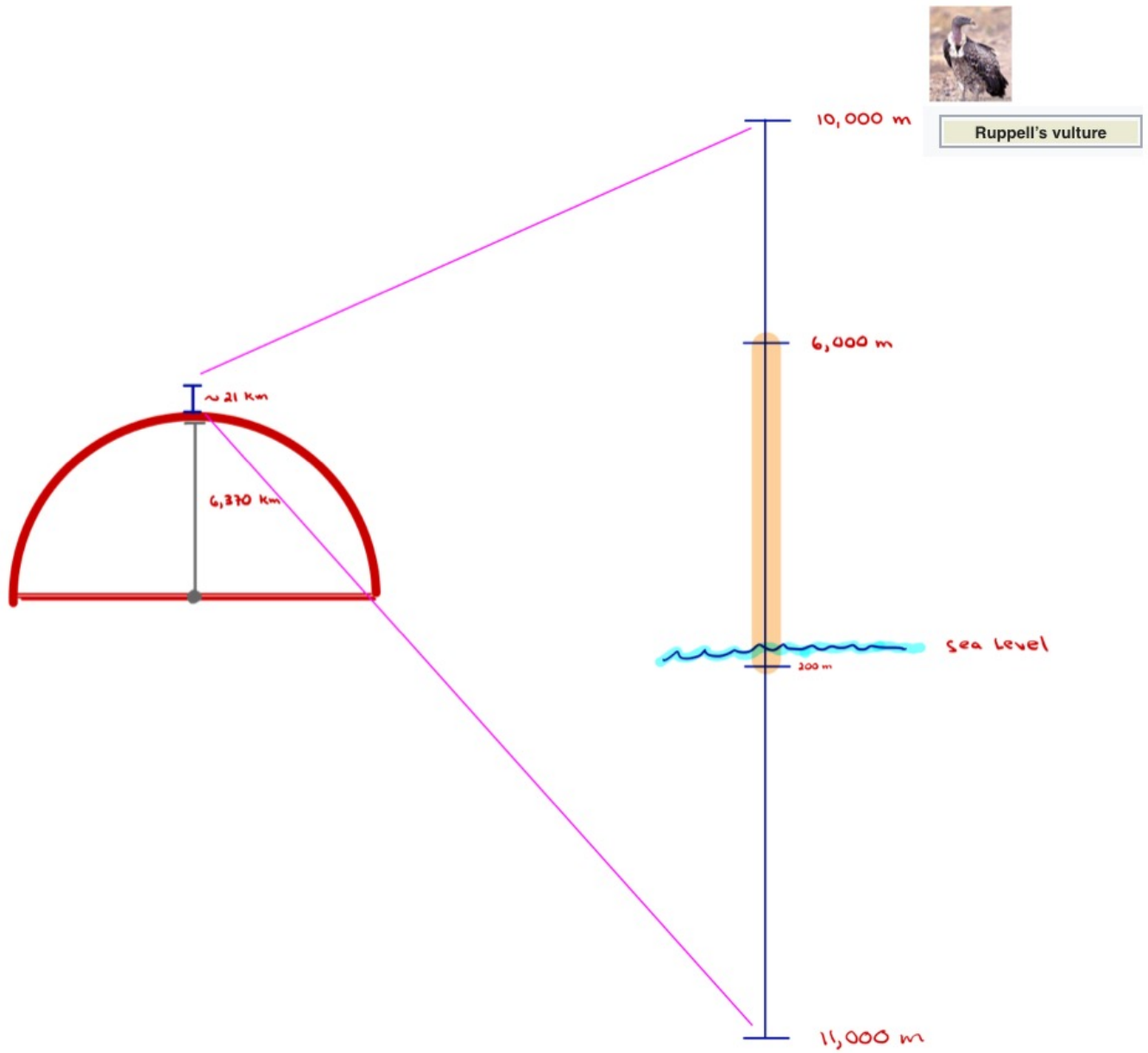


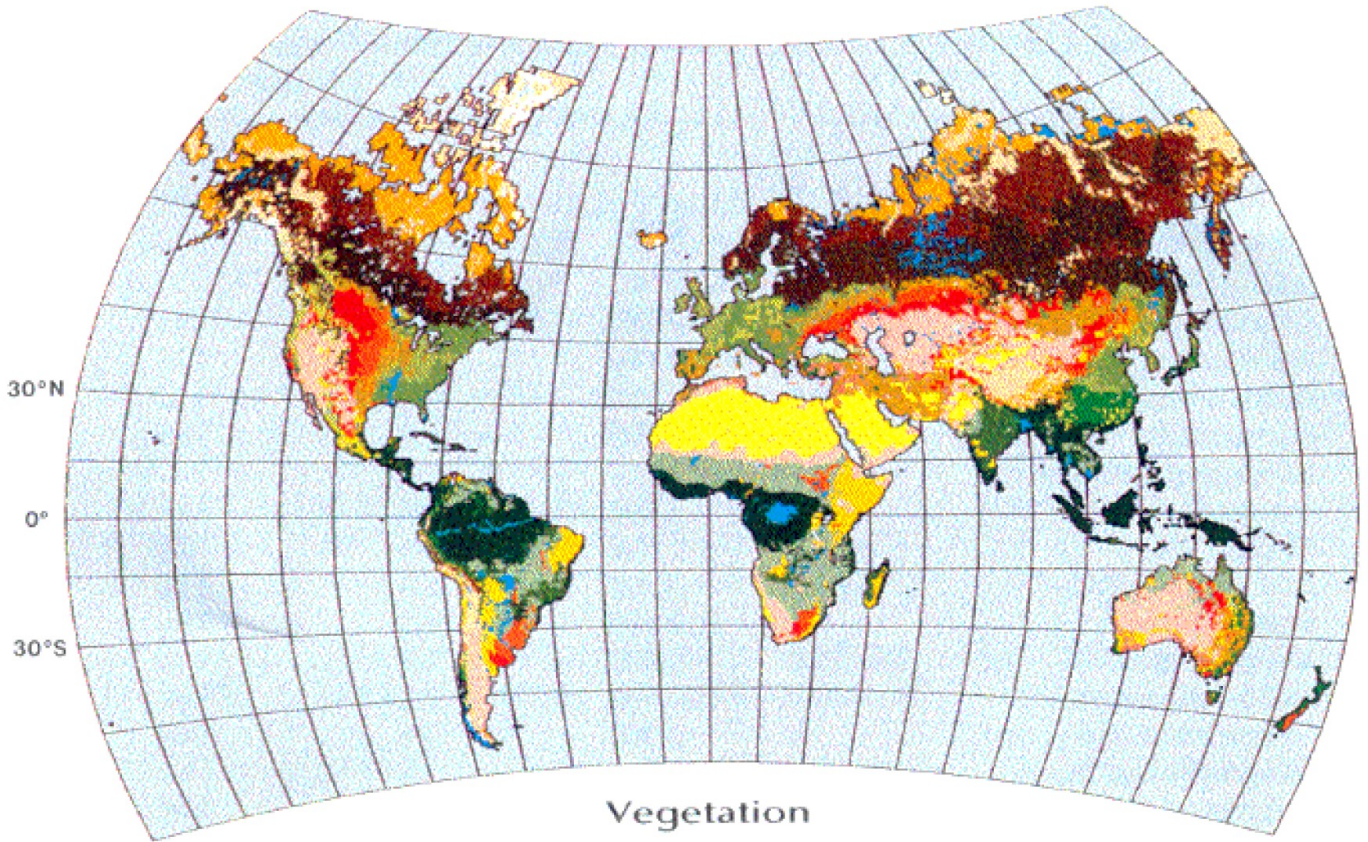
The Biosphere



















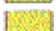



Ruppell's vulture



A hadal amphipod from 10,500 m the Sirena Deep collected on this expedition. Scale bar on left is in centimeters (cm). Close-up of head shows yellow patches that are thought to be rudimentary eyes, but the function of the red eye-like lobes is uncertain.



- | | | | | | |
|---|------------------|---|-------------------------------|---|-------------------------|
|  | Boreal Forest |  | Tropical Evergreen Forest |  | Short Grassland |
|  | Boreal Woodlands |  | Tropical Deciduous Forest |  | Tall Grassland |
|  | Wet Moist Tundra |  | Tropical Savanna |  | Mediterranean Shrubland |
|  | Polar Desert |  | Temp. Broad Leaf Evrg. Forest |  | Arid Shrubland |
|  | Ice |  | Temperate Mixed Forest |  | Temperate Savanna |
|  | Wetlands |  | Temperate Deciduous Forest |  | Xeromorphic Woodland |
| | |  | Temperate Coniferous Forest |  | Desert |

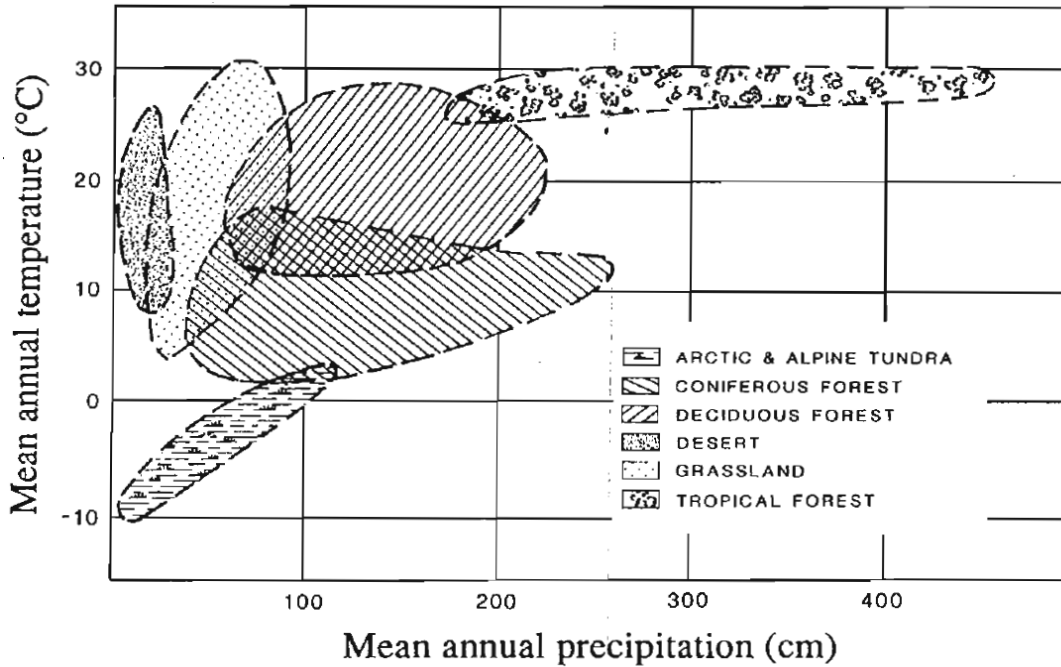


Fig. 5.14. Vegetation formations on the coordinate system defined by mean annual temperature and total annual precipitation. Redrawn from MacMahon (1981). Clark 1991 (in Wyman 1991)

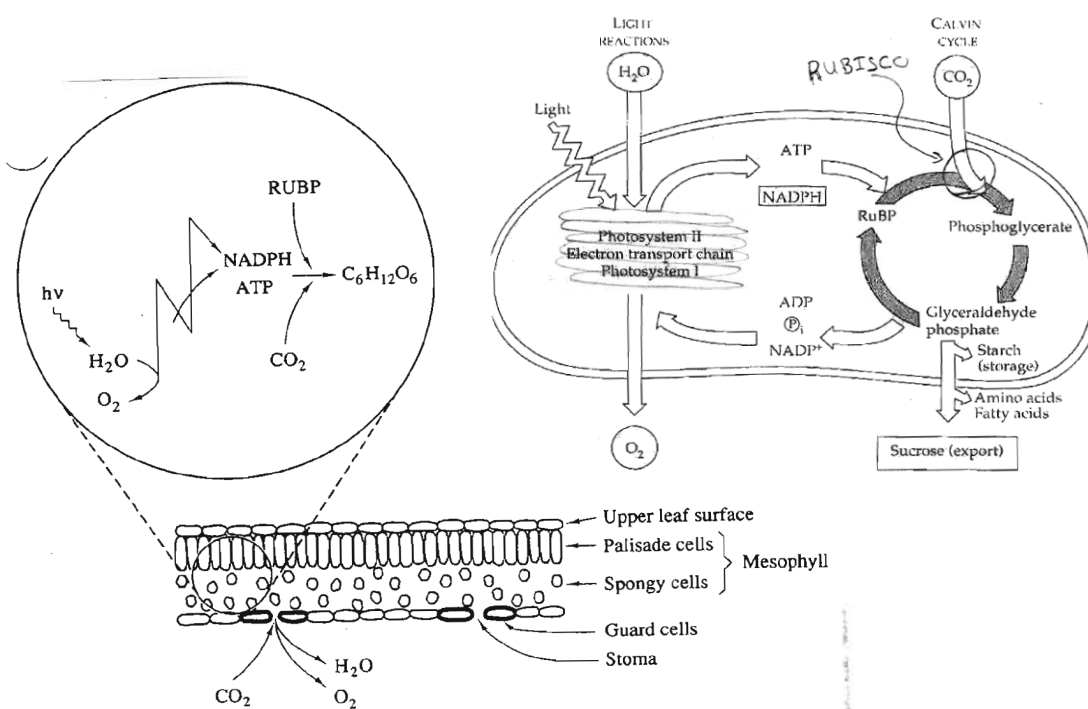


Figure 5.1 Cross-sectional view of a typical plant leaf, showing the upper (palisade) layer of cells, in which photosynthesis occurs, and guard cells, which control the diffusion of CO_2 (in) and H_2O and O_2 (out) through stomates on the lower surface. A summary of the photosynthetic reaction, occurring in the chloroplasts of the palisade cells is shown in the insert.

Figure 10.20 A summary of photosynthesis. This diagram outlines the main reactants and products of photosynthesis as it occurs in the chloroplasts of plant cells. The light reactions convert light energy into the chemical energy of ATP and NADPH. The pigment and protein molecules that carry out the light reactions are found in the thylakoid membranes and include the molecules of two photosystems and an electron transport chain. The light reactions split H_2O and release O_2 to Earth's atmosphere. The Calvin cycle, which takes place in the stroma of the chloroplast, uses ATP and NADPH to convert CO_2 to carbohydrate (three key compounds of the cycle are shown). The direct product of the Calvin cycle is the three-carbon sugar glyceraldehyde phosphate. Enzymes in the chloroplast and cytoplasm convert this small sugar to a diversity of other organic compounds. The Calvin cycle returns ADP, inorganic phosphate, and NADP^+ to the light reactions. The entire ordered operation depends on the structural integrity of the chloroplast and its membranes.

Microbial life and biogeochemical cycling on land 3,220 million years ago

Martin Homann^{1*}, Pierre Sansjofre¹, Mark Van Zuilen², Christoph Heubeck³, Jian Gong², Bryan Killingsworth¹, Ian S. Foster¹, Alessandro Airo⁴, Martin J. Van Kranendonk⁵, Magali Ader² and Stefan V. Lalonde¹

The colonization of emergent continental landmass by microbial life was an evolutionary step of paramount importance in Earth history. Here we report direct fossil evidence for life on land 3,220 million years ago (Ma) in the form of terrestrial microbial mats draping fluvial conglomerates and gravelly sandstones of the Moodies Group, South Africa. Combined field, petrographic, carbon isotope and Raman spectroscopic analyses confirm the synsedimentary origin and biogenicity of these unique fossil mats as well as their fluvial habitat. The carbon isotope compositions of organic matter ($\delta^{13}\text{C}_{\text{org}}$) from these mats define a narrow range centred on -21‰ , in contrast to fossil mats of marine origin from nearby tidal deposits that show $\delta^{13}\text{C}_{\text{org}}$ values as low as -34‰ . Bulk nitrogen isotope compositions ($2 < \delta^{15}\text{N} < 5\text{‰}$) are also significantly different from their marine counterparts ($0 < \delta^{15}\text{N} < 3\text{‰}$), which we interpret as reflecting denitrification in the terrestrial habitat, possibly of an atmospheric source of nitrate. Our results support the antiquity of a thriving terrestrial biosphere during the Palaeoarchaeon and suggest that a complex and microbially driven redox landscape existed during the deposition of the Moodies Group, with distinct biogeochemical cycling occurring on land by 3,220 Ma.

PHYLOGENETICS

Global aerobics before Earth's oxygenation

Phylogenetic analysis of oxygen-utilizing and -producing enzymes indicates an early emergence of an oxygenated biosphere, providing phylogenetic insight into a question that has more commonly been approached from the basis of fossils and geochemical tracers.

Noah J. Planavsky and Daniel B. Mills

The emergence of biological oxygen (O_2) production irreversibly transformed Earth's biosphere. Without this one-off metabolic innovation, life on Earth would be exclusively microbial, and animal life would be impossible. Despite the importance of this evolutionary singularity, there is no consensus regarding when it first occurred. At a minimum, oxygenic photosynthesis must have evolved by ~ 2.4 billion years ago, when geological evidence overwhelmingly indicates that oxygen became a permanent feature of the atmosphere¹. The geologically youngest estimates for the origin of oxygenic photosynthesis place it close in time to this rise of oxygen². If true, these estimates suggest that Earth's oxygenation was immediately controlled by the evolution of oxygenic photosynthesis itself. In contrast, other estimates place the appearance of photosynthetic oxygen production hundreds of millions of years before the oxygenation of the atmosphere^{3,4}. These geologically older estimates imply that geological processes ultimately controlled the timing of Earth's oxygenation. These competing narratives paint two very different pictures of how and why our planet became oxygenated, and, accordingly, very different predictions concerning when oxygen first became widely available to life on Earth. Writing in *Nature Ecology & Evolution*, Jabłońska and Tawfik⁵ provide phylogenetic evidence supporting the early — over 3 billion years ago — emergence of an oxygen-producing and -utilizing biosphere.

Three main lines of evidence have been used to try to pinpoint the origin of oxygen-producing photosynthesizers: fossils, geochemical tracers and molecular data. Palaeontologists have used fossils to tackle this question for decades. This work has led to compelling evidence for the early emergence of life — well over 3 billion years ago (for example, ref. ⁶). However, the earliest fossils are too morphologically simple and uninformative to reliably infer any taxonomic affinity and/or metabolic capacity. The basic rationale behind using

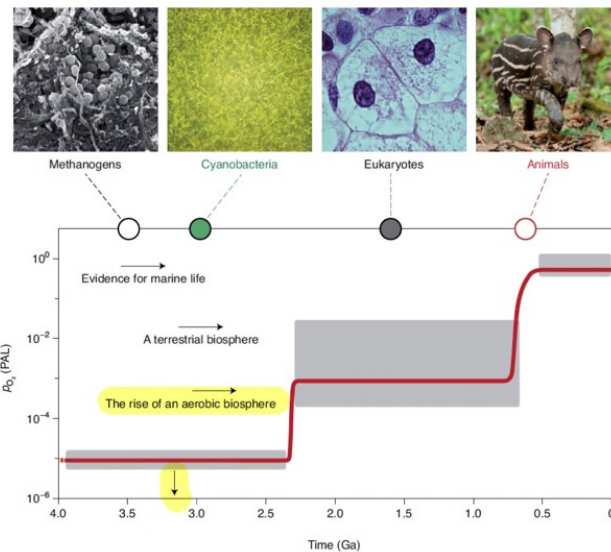
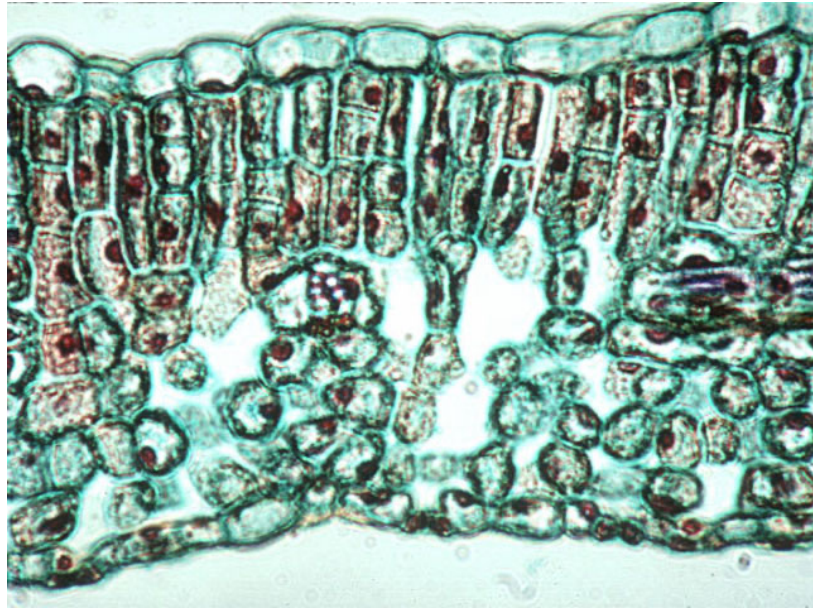


Fig. 1 | A timeline of the key biological evolution events in Earth's history. Recent phylogenetic and geochemical evidence support that the rise of an oxygen-utilizing biosphere occurred over 3 billion years ago — well before the Earth permanently transitioned to having an oxygenated atmosphere. Ga, billion years ago; PAL, present atmospheric level. Figure based on ref. ¹⁰. Credit: Zohaib Ur Rehman Afridi / Alamy Stock Photo (methanogens); Christopher Boswell / Alamy Stock Photo (cyanobacteria); Ed Reschke / Stone / Getty (eukaryotes); Ben Queenborough / Alamy Stock Photo (animals)

geochemical tools to track the evolution of oxygenic photosynthesis is straightforward — oxygenic photosynthesis is the only appreciable source of O_2 to Earth's surface and therefore the chemical record of free oxygen can potentially be used as a robust biosignature. Over the past decade there has been a flurry of reports of geochemical evidence for the early emergence of oxygenic photosynthesis. However, whether these signals truly require free oxygen and whether they are faithful archives of

palaeoenvironmental conditions billions of years ago has been hotly debated^{7,8}. Molecular records have also been extensively used to reconstruct the evolution of photosynthesis. But estimates of when oxygenic photosynthesis first evolved using molecular sequence data span a tremendous range — limiting, at face value, their utility to resolve ongoing debates about the timing of this evolutionary event.

Jabłońska and Tawfik leverage proteomics to provide a new perspective



A_{ci} Curve

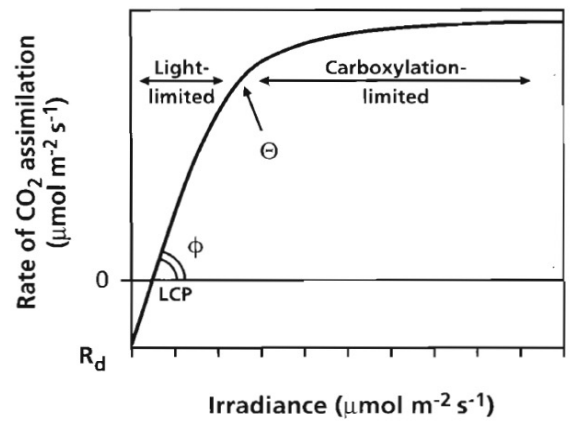
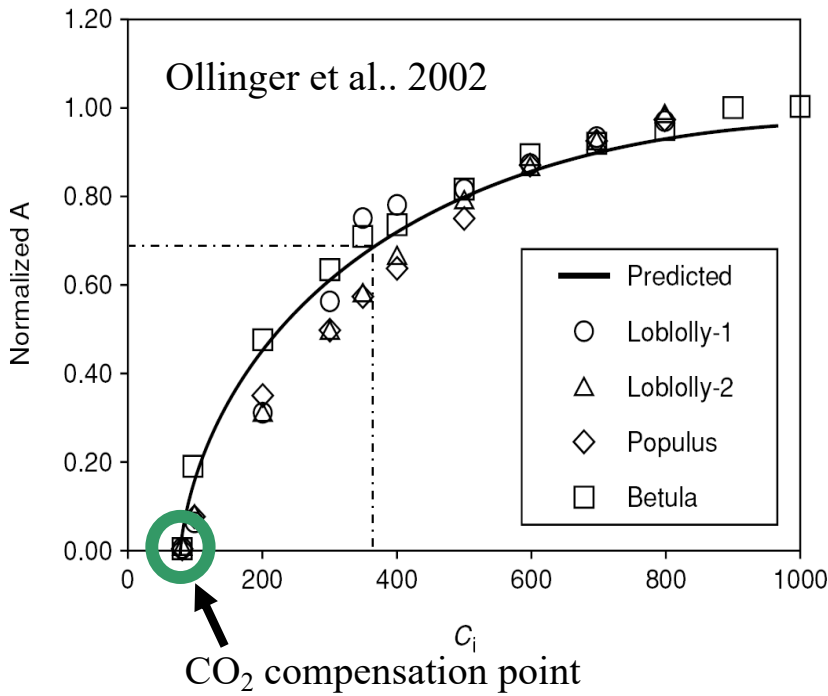


FIGURE 8. Typical response of photosynthesis to irradiance, drawn according to Equation 6 in the text. The intercept with the x-axis is the light-compensation point (LCP), the initial slope of the line gives the quantum yield (ϕ) and the intercept with the y-axis is the rate of dark respiration (R_d). The curvature of the line is described by θ . At low irradiance, the rate of CO₂ assimilation is light-limited; at higher irradiance A is carboxylation limited. A_{max} is the light-saturated rate of CO₂ assimilation at ambient p_a .

Lambers et al. 1998

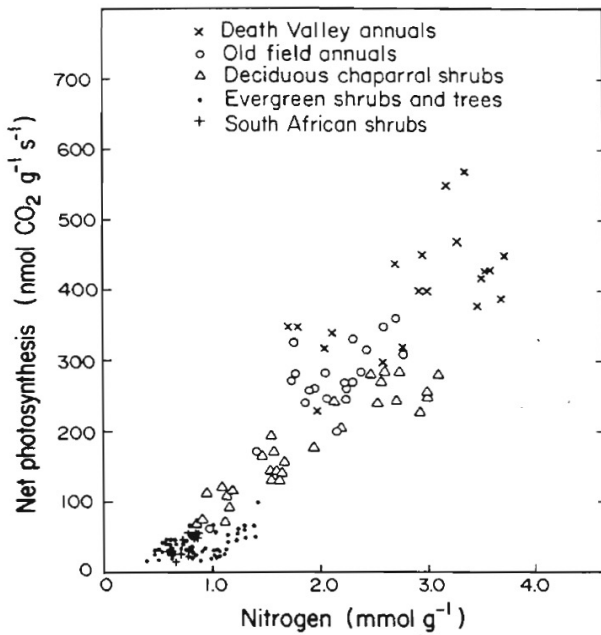


Figure 1.2. A_{max} -N relationships for the VINE survey, representing 21 species grown under natural conditions. A_{max} was measured in the field. N was determined with a micro-Kjeldahl assay on the same leaves used for the photosynthesis measurements. A_{max} and N are both expressed on a leaf-weight basis. $A_{max} = -76.1 + 149 \cdot N$, $n = 137$, $r = 0.92$, $P < 0.001$.

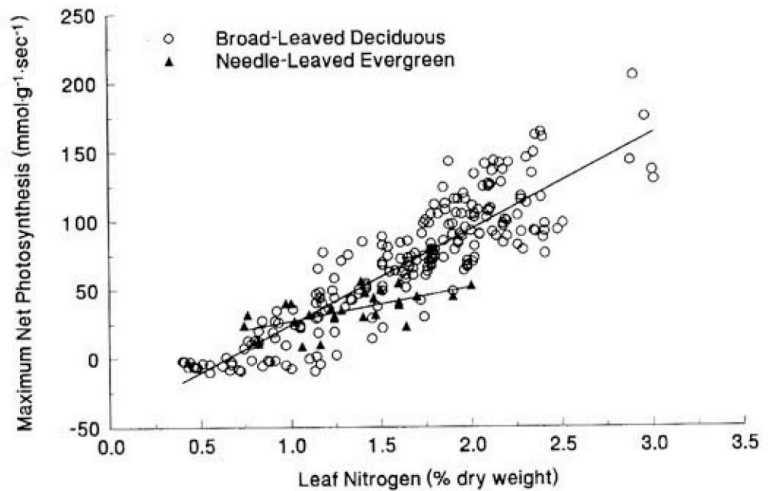


Fig. 2 Relationship between foliar N concentration and A_{max} for broad-leaved deciduous and needle-leaved evergreen species (data from Reich et al. 1995)

Aber et al. 1996

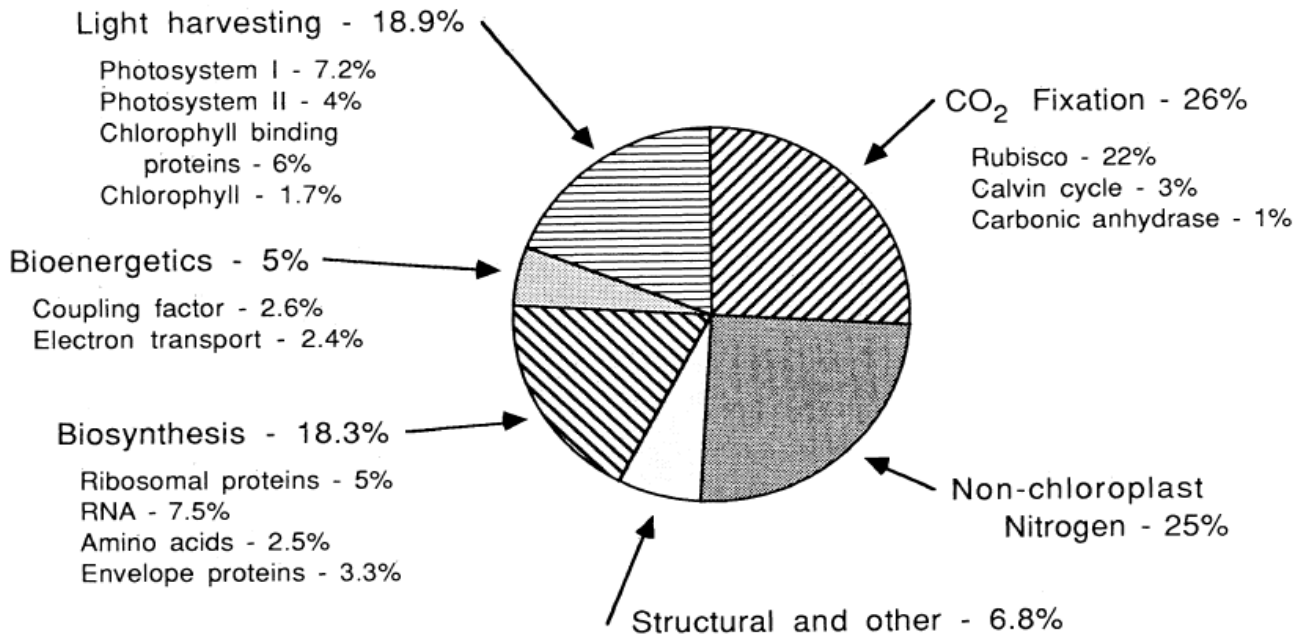


Figure 1. The proportional allocation of leaf nitrogen in a sun leaf of a plant with C₃ photosynthesis. The photosynthetic compartments are those labeled light harvesting, CO₂ fixation, and bioenergetics. Data from Evans (1983 and unpublished); figure courtesy of J. R. Seemann, Desert Research Institute, Reno, NV.

Chapin et al. 1987

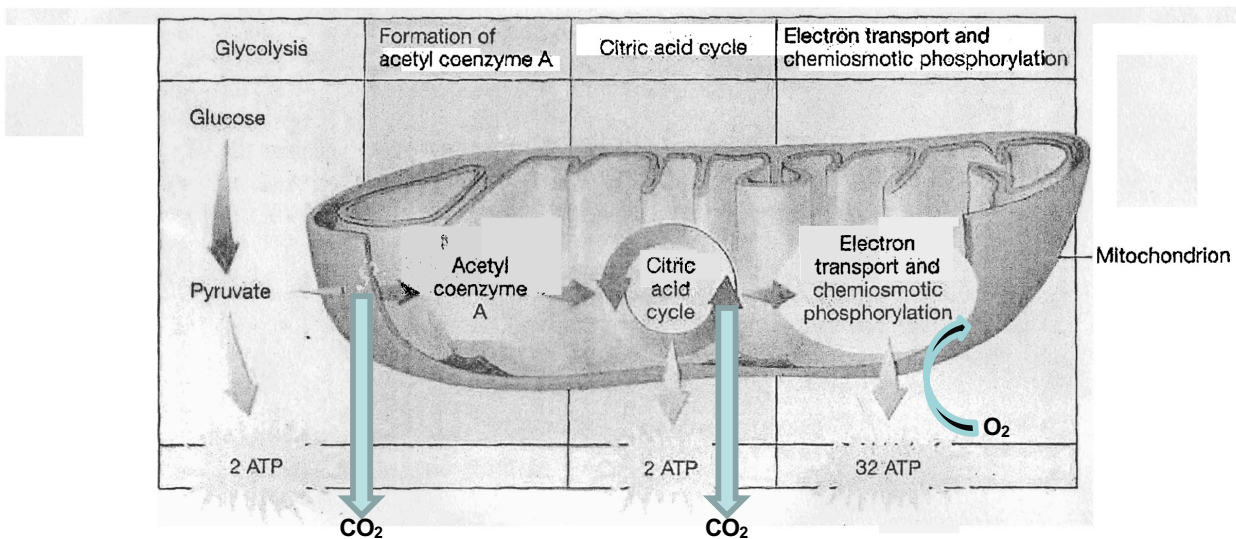
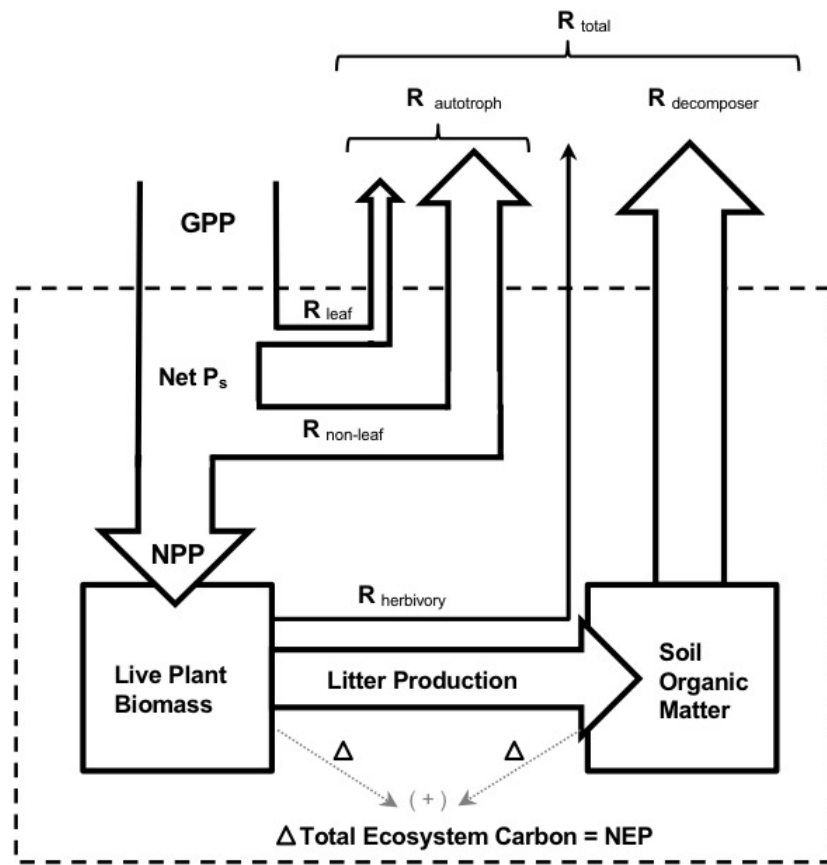


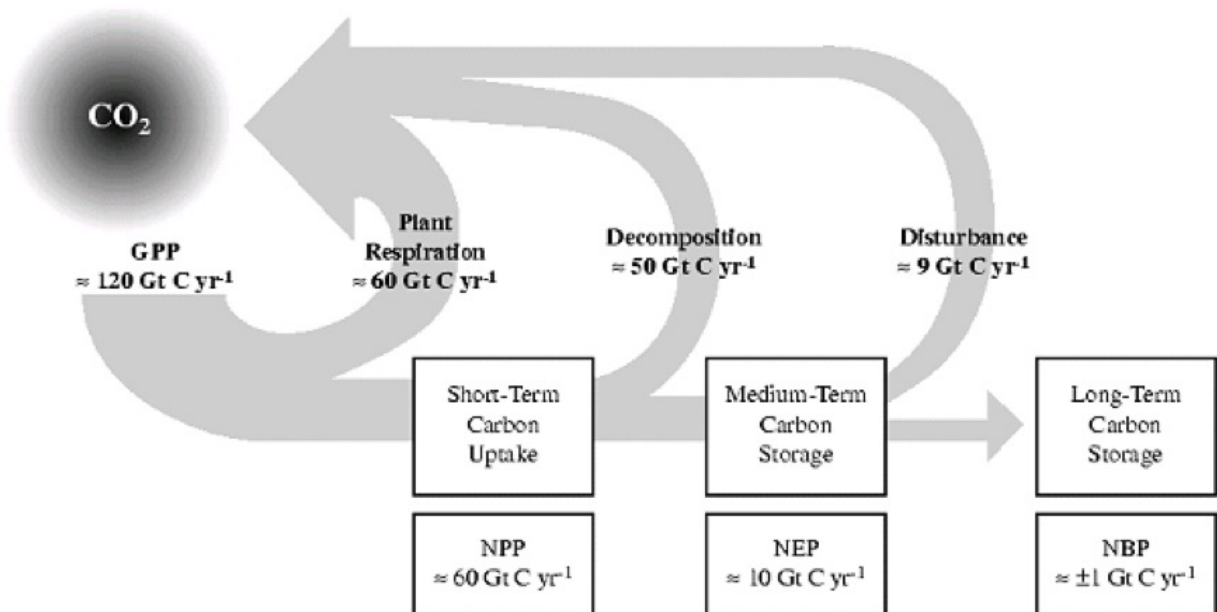
Figure 7-4 Four main phases in aerobic respiration are (1) glycolysis, (2) the formation of acetyl coenzyme A from pyruvate, (3) the citric acid cycle, and (4) the electron transport system and chemiosmosis. Glycolysis occurs in the cytosol. Pyruvate, the

product of glycolysis, enters a mitochondrion, where cellular respiration continues. Most ATP is synthesized during electron transport/chemiosmosis.



$$NPP = GPP - R_{\text{autotroph}} = R_{\text{herbivory}} + \text{Litter Production} + \underbrace{\text{Change in Live Biomass}}_{\text{True Increment}}$$

$$NEP = \underbrace{GPP - R_{\text{autotroph}}}_{NPP} - \underbrace{R_{\text{herbivory}} - R_{\text{decomposer}}}_{R_{\text{heterotroph}}}$$



Biome	Area (10 ⁶ km ²)	NPP (g C m ⁻² yr ⁻¹)	Total NPP (10 ¹⁵ g C yr ⁻¹)	Biomass (g C m ⁻²)	Total plant C pool (10 ¹⁵ g C)
Tropical forests	17.5	1250	20.6	19,400	320
Temperate forests	10.4	775	7.6	13,350	130
Boreal forests	13.7	190	2.4	4150	54
Mediterranean shrublands	2.8	500	1.3	6000	16
Tropical savannas/grasslands	27.6	540	14.0	2850	74
Temperate grasslands	15.0	375	5.3	375	6
Deserts	27.7	125	3.3	350	9
Arctic tundra	5.6	90	0.5	325	2
Crops	13.5	305	3.9	305	4
Ice	15.5				
Total	149.3		58.9		615

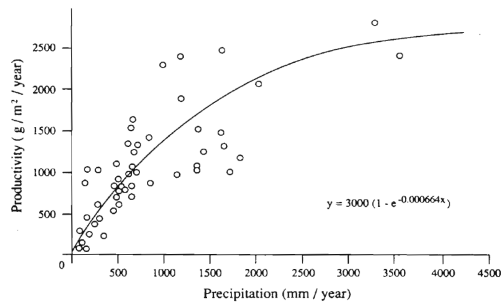


Figure 5.9 Relationship between NPP and mean annual precipitation for 52 locations around the world. From Lieth (1975).

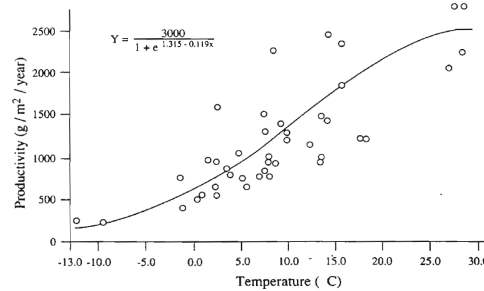


Figure 5.8 Relationship between NPP determined by harvest and mean annual temperature for 52 studies on various continents. From Lieth (1975).

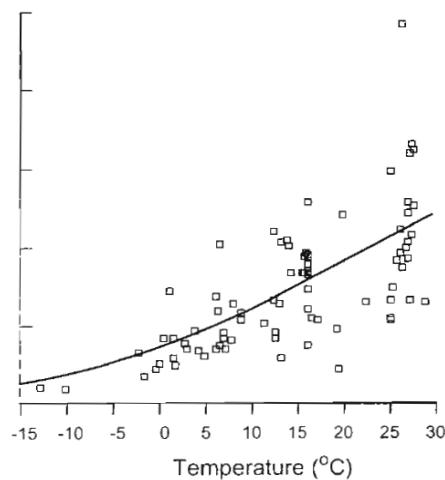
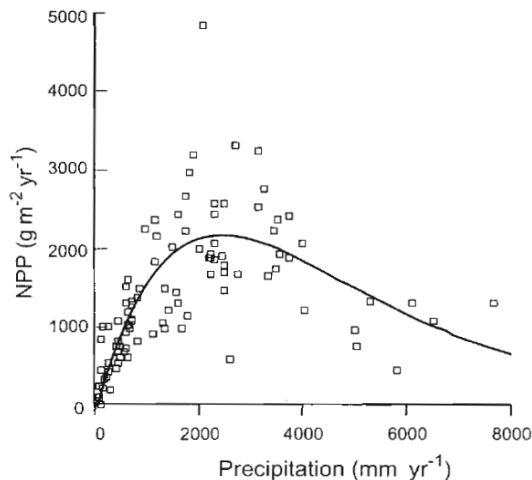
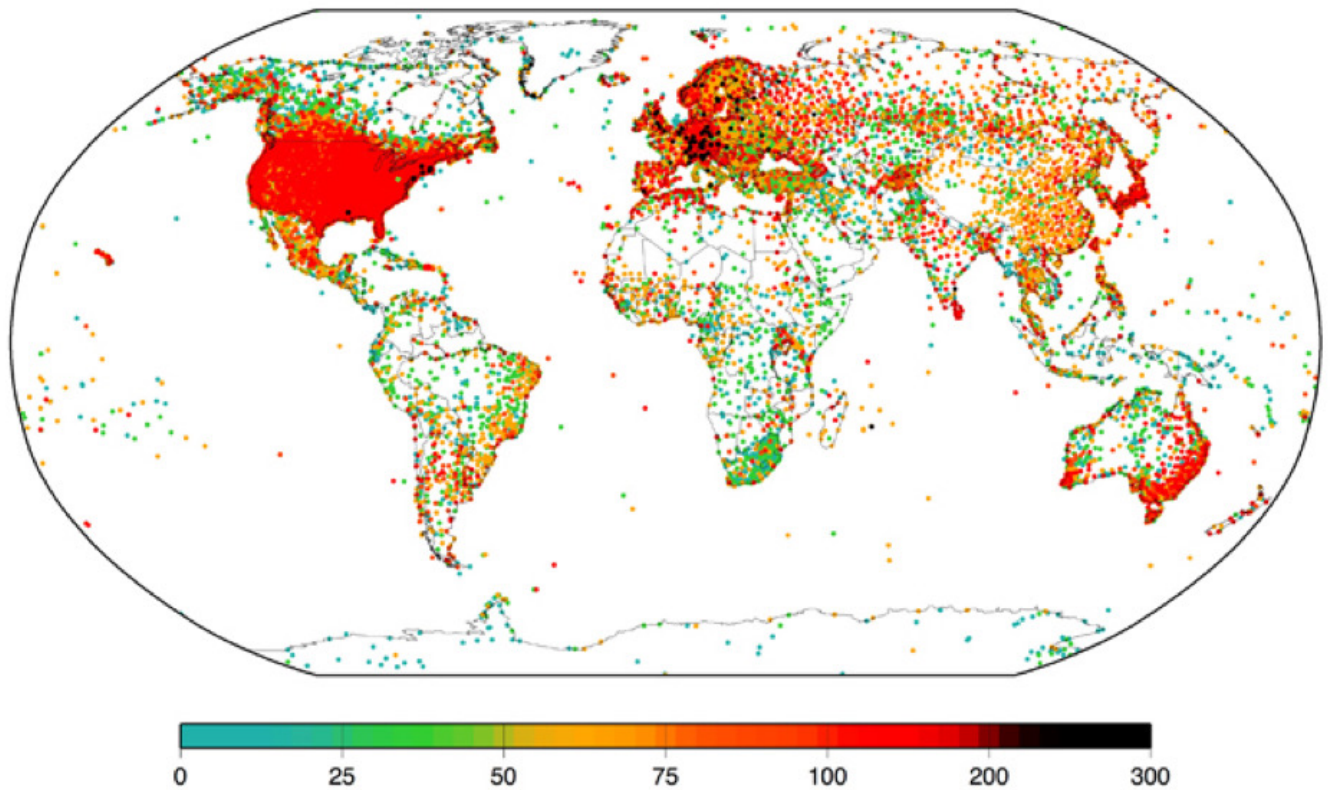


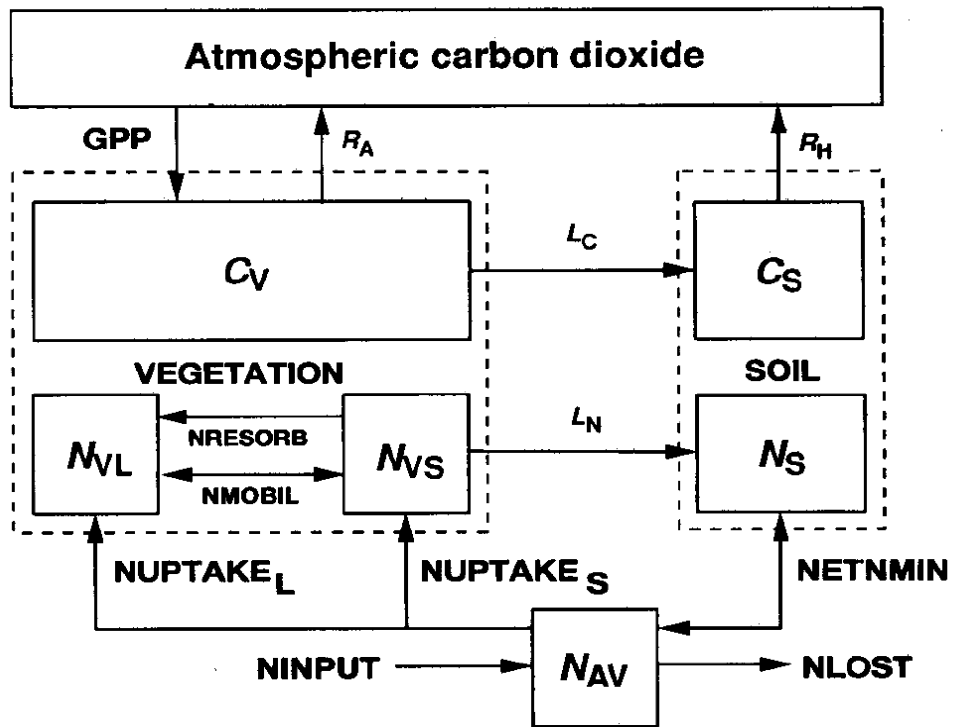
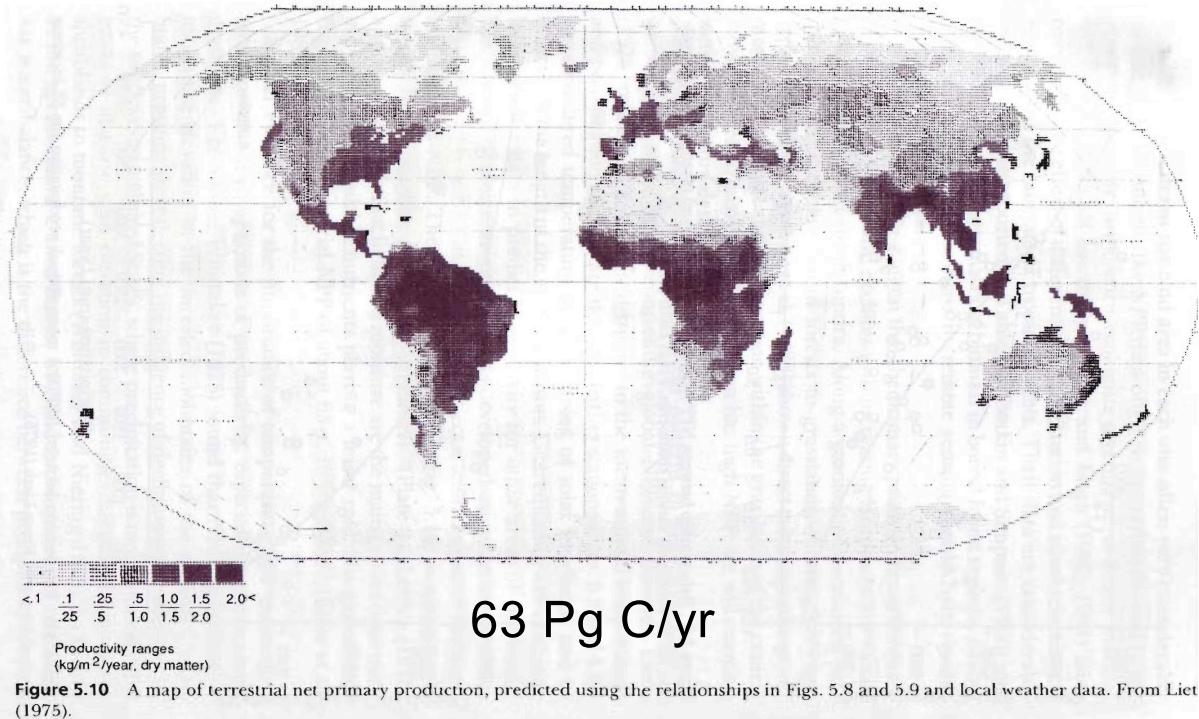
FIGURE 6.3. Correlation of NPP (in units of biomass) with temperature and precipitation. NPP is greatest in warm moist environments such as tropical forests and lowest in cold or dry ecosystems such as tundra and deserts. In tropical forests, NPP declines at extremely

high precipitation (>3 m yr⁻¹), due to indirect effects of excess moisture, such as low soil oxygen and loss of nutrients through leaching. (Figure modified from Schuur Unpublished; data from Lieth 1975, Clark et al. 2001b, and Schuur et al. 2001.)

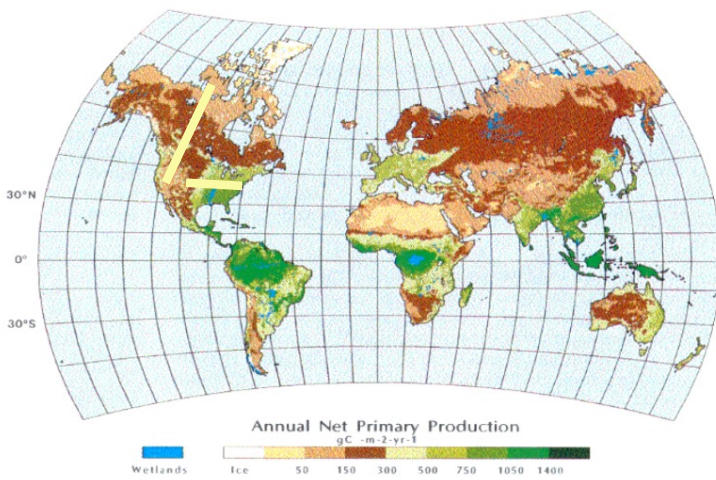
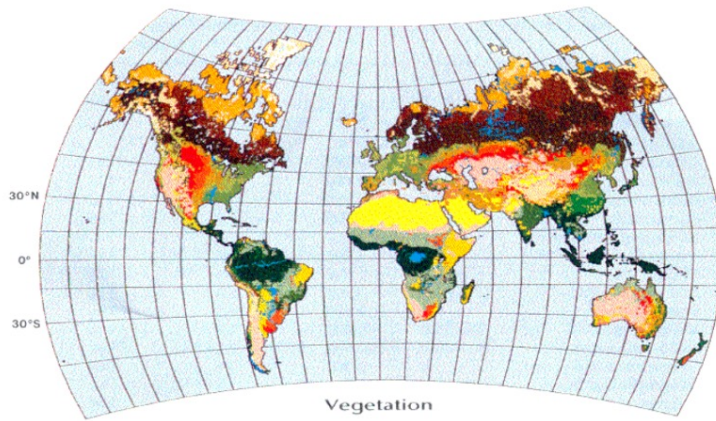


The geographical locations of the 30,000 weather station records held in the ISTI databank. The colour of the dots shows the length of the station record, with many records exceeding 100 years (red) and some even exceeding 200 years old (black).

www.npl.co.uk/news/weather-station-data-available-to-all

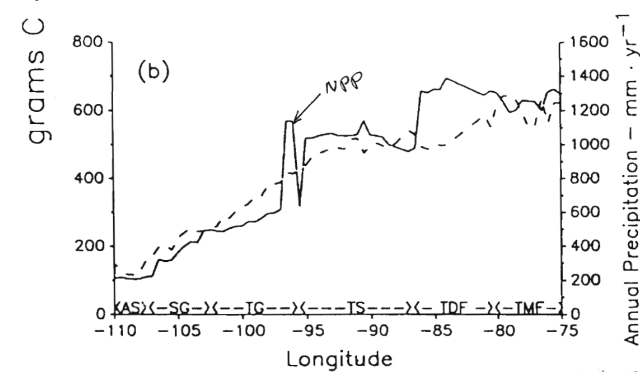
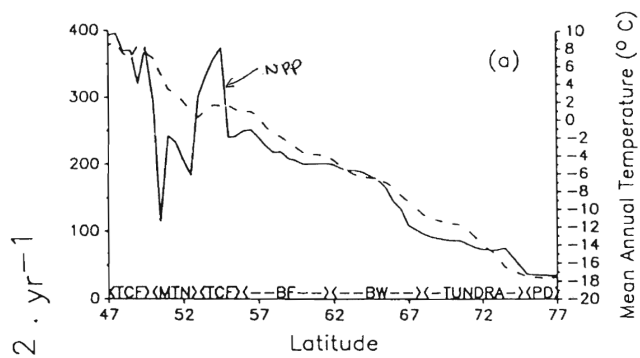


Melillo et al. 1993



53.3 Pg C/yr

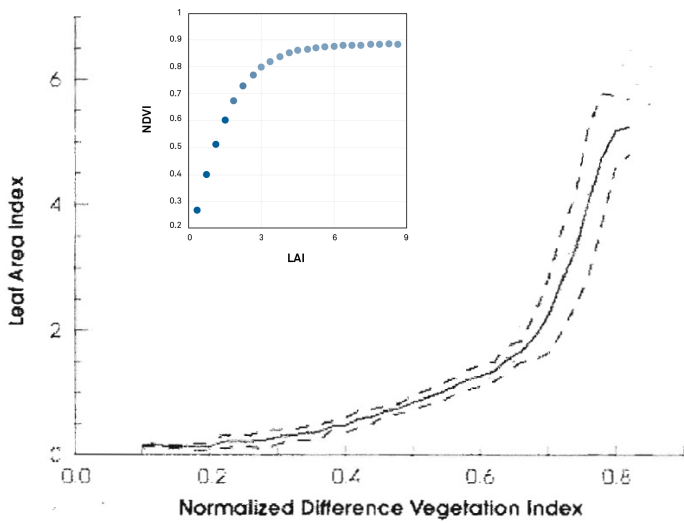
Melillo et al. 1993



McGuire et al. 1992

Satellite-Based Methods

Passive Sensors Using Reflected Light



Leaf Area Index (LAI) is related to, but not directly proportional to, Normalized Difference Vegetation Index (NDVI). In addition, different vegetation types (broadleaf evergreens versus needleleaf evergreens, for example) and soil types exhibit different relationships between the two parameters. The graph at left compares NDVI to LAI. Unfortunately, the relationship between NDVI and LAI is not unique (multiple values of NDVI correspond to a single LAI value), a problem which is being addressed by the current generation of satellite instruments, such as the Moderate-Resolution Imaging Spectroradiometer (MODIS). [Graph courtesy Wolfgang Buermann, Boston University [Climate and Vegetation Research Group](#).]

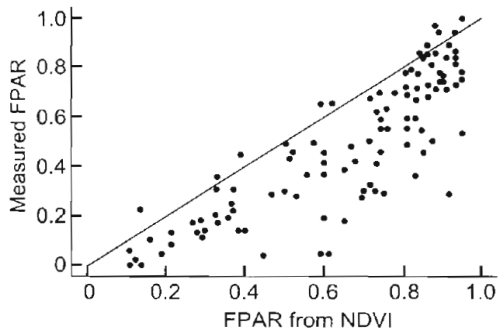


FIGURE 5.19. Relationship between the fraction of photosynthetically active radiation (FPAR) absorbed by vegetation estimated from satellite measurements of NDVI (x-axis) and FPAR measured in the field (y-axis). Data were collected from a wide range of ecosystems, including temperate and tropical grasslands and temperate and boreal conifer forests. Satellites provide an approximate measure of the photosynthetically active radiation absorbed by vegetation and therefore the carbon inputs to ecosystems. (Redrawn with permission from *Journal of Hydrometeorology*; Los et al. 2000.)

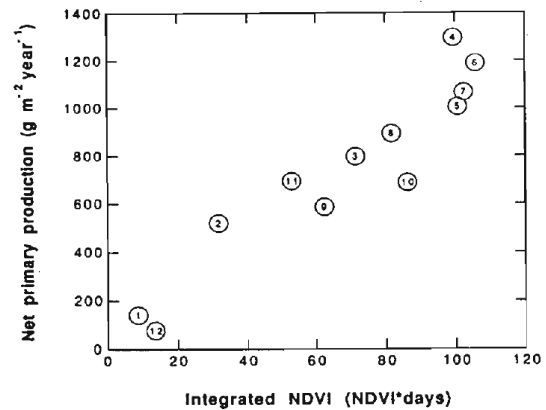


Figure 8 Relationship between mean net primary productivity for several biomes and the seasonally integrated normalized difference vegetation index (NDVI) from the AVHRR sensor. The primary productivity values are published estimates considered representative for (1) tundra, (2) tundra-coniferous ecotone, (3) boreal coniferous, (4) temperate moist coniferous, (5) coniferous-deciduous ecotone, (6) deciduous, (7) oak-pine subclimax, (8) pine subclimax, (9) grassland, (10) cultivated, (11) woodland and scrub, and (12) desert. [Redrawn from *Goward et al. (1985)*.]

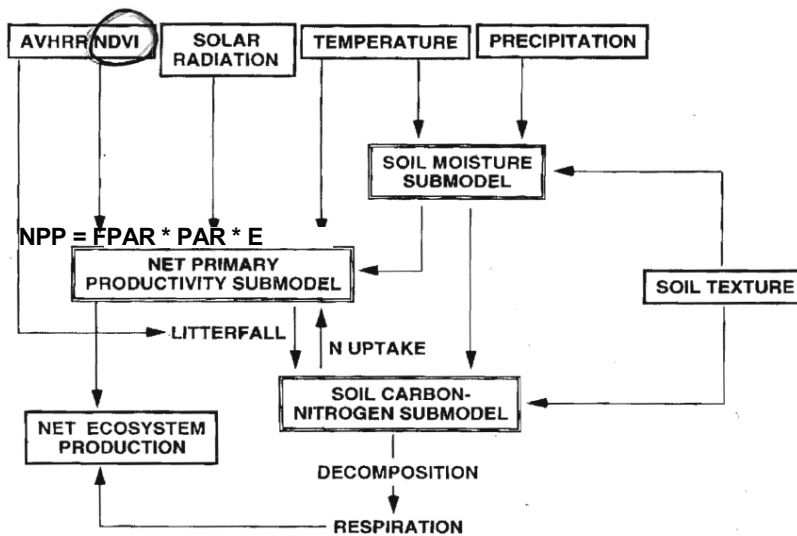


Fig. 1. Model integration framework. Global climate data sets are combined with soil texture settings to compute the monthly water balance, which controls NPP and soil microbial activity.

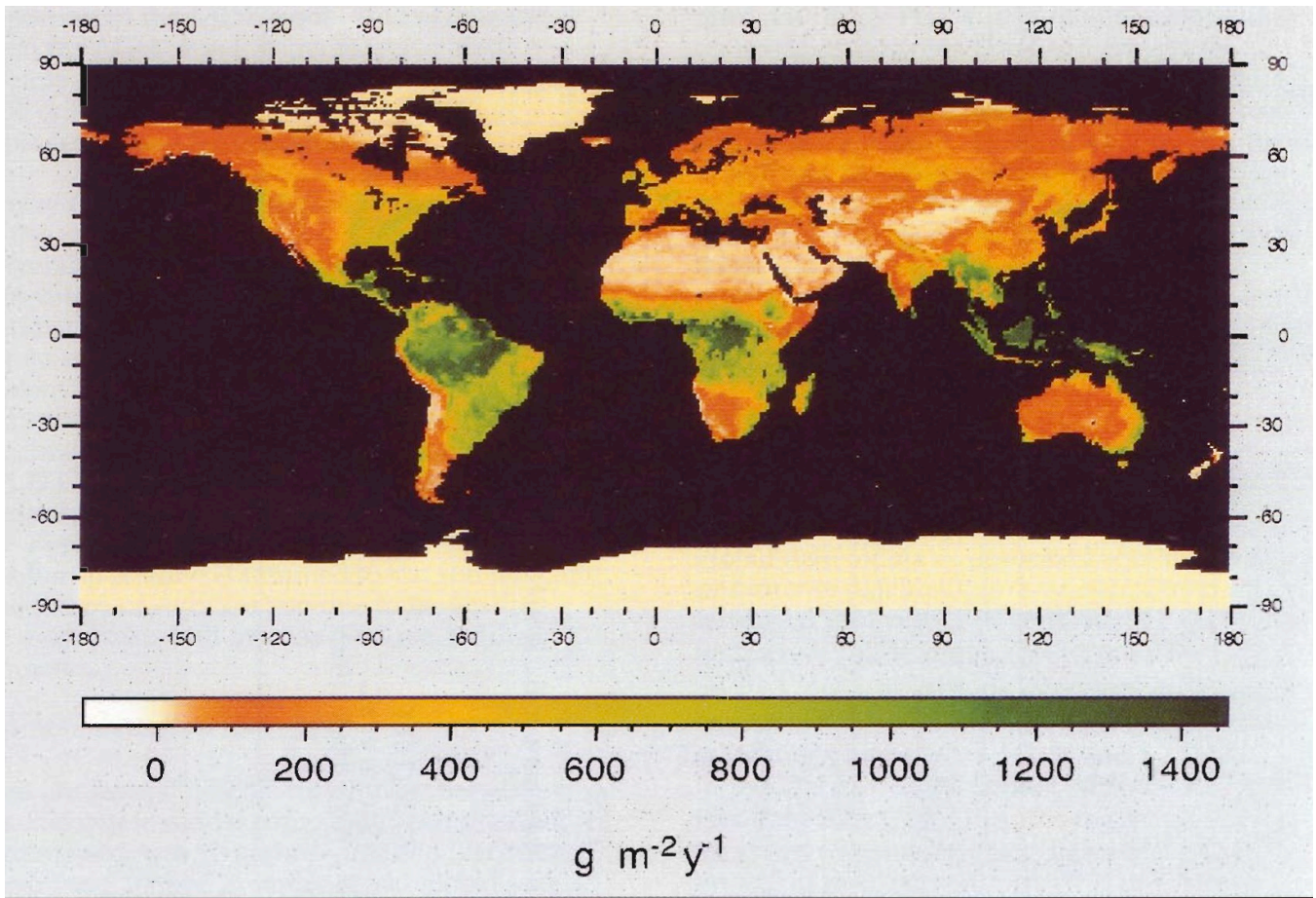
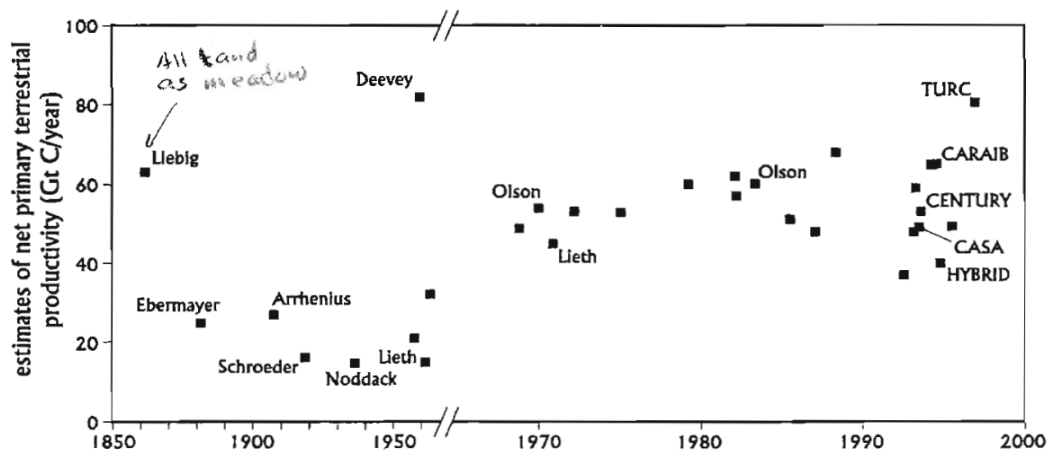


Plate 2. Global map of NPP computed according to the model in equation (1).

https://www.youtube.com/watch?v=OK_HI3sjbtI

48 Pg C/yr

Potter et al. 1993



7.5 Nearly 150 years of estimates of global annual NPP show most of the totals within the range of 50–70 Gt C per year.

Satellite-Based Methods

Passive Sensors Using Emitted Light

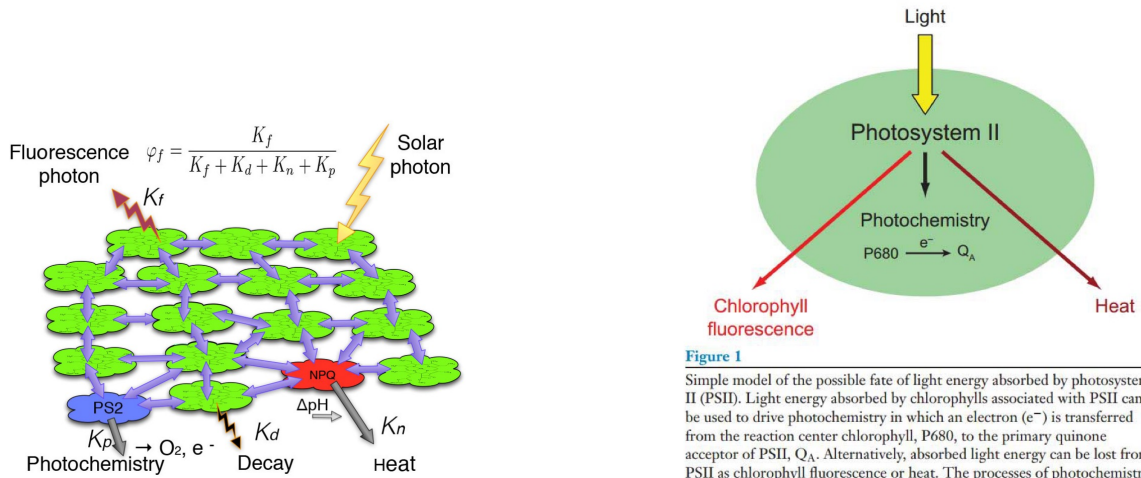


Figure 1

Simple model of the possible fate of light energy absorbed by photosystem II (PSII). Light energy absorbed by chlorophylls associated with PSII can be used to drive photochemistry in which an electron (e⁻) is transferred from the reaction center chlorophyll, P680, to the primary quinone acceptor of PSII, Q_A. Alternatively, absorbed light energy can be lost from PSII as chlorophyll fluorescence or heat. The processes of photochemistry, chlorophyll fluorescence, and heat loss are in direct competition for excitation energy. If the rate of one process increases the rates of the other two will decrease.

Annu. Rev. Plant Biol. 2008.59:89-113.

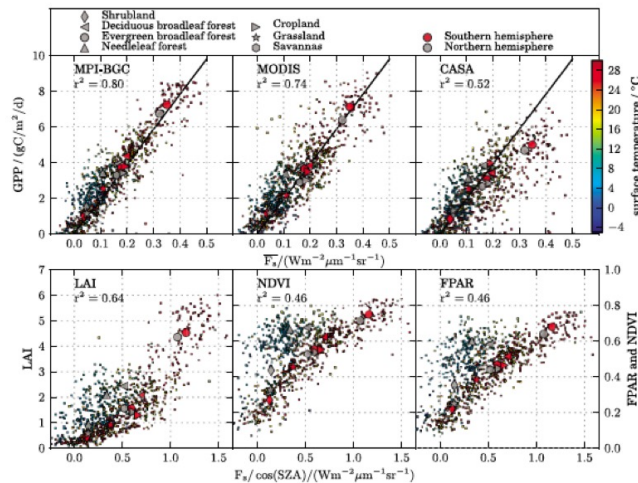
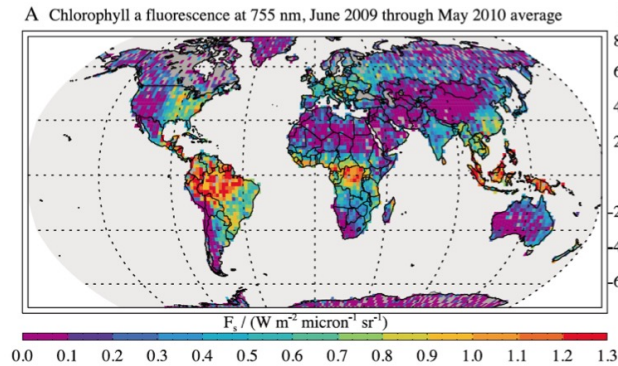


Figure 2. (top) Scatter-plot of $4^\circ \times 4^\circ$ grid cell averages of fluorescence (F_a) vs. GPP model estimates (small dots colored by latitude, only grid boxes over vegetated areas and with a 1- σ precision error in F_a of $<0.04 \text{ W m}^{-2} \mu\text{m}^{-1} \text{ sr}^{-1}$ are shown). The linear regression line in all panels equals a linear fit through the origin on the basis of the MPI-BGC GPP model. (bottom) Normalized $F_a/\cos(\text{SZA})$ vs. MODIS LAI, NDVI and FPAR. The large symbols in all plots are biome averages, further separated for northern and southern hemisphere and based on 1x1° biome classification see auxiliary material.

CARBON CYCLE

OCO-2 advances photosynthesis observation from space via solar-induced chlorophyll fluorescence

Y. Sun,^{1*}† C. Frankenberg,^{2,1*} J. D. Wood,³ D. S. Schimel,¹ M. Jung,⁴ L. Guanter,⁵ D. T. Drewry,^{1,6} M. Verma,⁷ A. Porcar-Castell,⁸ T. J. Griffis,⁹ L. Gu,¹⁰ T. S. Magney,¹ P. Köhler,² B. Evans,¹¹ K. Yuen¹

Quantifying gross primary production (GPP) remains a major challenge in global carbon cycle research. Spaceborne monitoring of solar-induced chlorophyll fluorescence (SIF), an integrative photosynthetic signal of molecular origin, can assist in terrestrial GPP monitoring. However, the extent to which SIF tracks spatiotemporal variations in GPP remains unresolved. Orbiting Carbon Observatory-2 (OCO-2)'s SIF data acquisition and fine spatial resolution permit direct validation against ground and airborne observations. Empirical orthogonal function analysis shows consistent spatiotemporal correspondence between OCO-2 SIF and GPP globally. A linear SIF-GPP relationship is also obtained at eddy-flux sites covering diverse biomes, setting the stage for future investigations of the robustness of such a relationship across more biomes. Our findings support the central importance of high-quality satellite SIF for studying terrestrial carbon cycle dynamics.

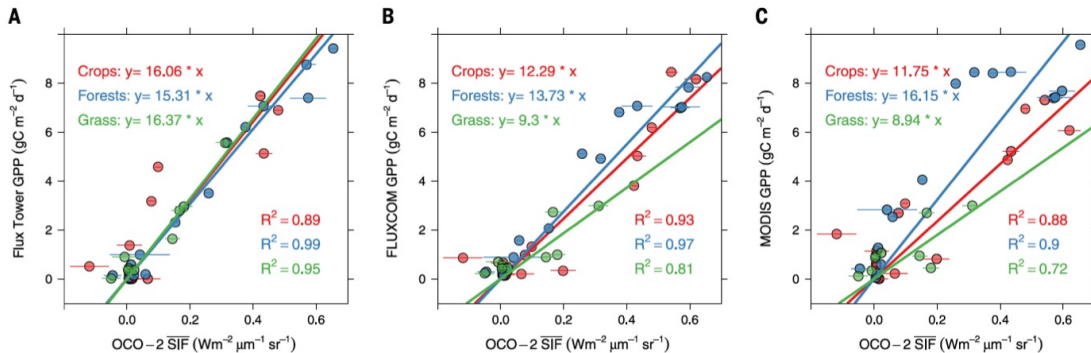


Fig. 3. SIF-GPP relationships. The relationship between GPP and OCO-2 SIF (daily mean value, denoted as $\overline{\text{SIF}}$, converted from instantaneous measurements) at three flux tower sites representative of three different biomes: crops (Minnesota Tall Tower KCMP) (30), grass (Stuart Plain in Australia) (31), and deciduous temperate forests [Missouri Ozark site (US_MOz)]. The first two sites are selected because they are in the direct underpass of OCO-2 orbital tracks; for the US_MOz site, OCO-2 SIF retrievals are obtained from representative forests in the vicinity of the tower. The KCMP footprint covers a mixture of corn, soybean, and grasses but is dominated by the two major crops. Error bars represent the SE of

the OCO-2 SIF retrieval. Daily GPP in the 2015 growing season is obtained during the OCO-2 overpasses from (A) eddy covariance measurements, (B) FLUXCOM products, and (C) MODIS products, sampled at these three flux sites. Both FLUXCOM and MODIS GPP are 8-day products and are linearly interpolated to the OCO-2 overpass dates. The site-specific FLUXCOM GPP value is extracted from the grid cell (0.083° by 0.083°) that corresponds to the latitude and longitude of the tower location. The site-specific MODIS (MOD17A2) GPP value is the average of nine adjacent pixels (1 km by 1 km) centered at the tower location. Both are roughly equivalent to ~9-km² area.

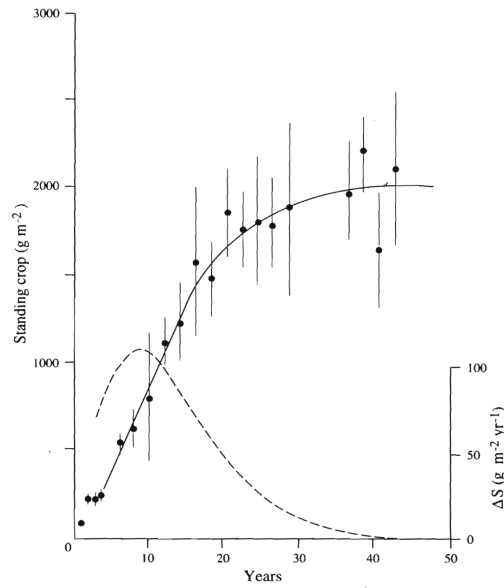
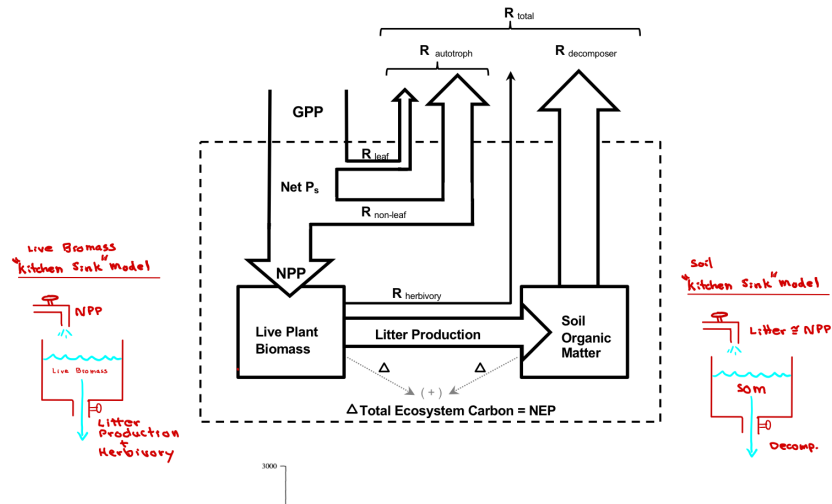


Figure 5.12 Biomass (solid line) and true increment (short dashes) of the aboveground components of a *Calluna* shrubland during 50 yr of recovery after fire. From Chapman et al. (1975).

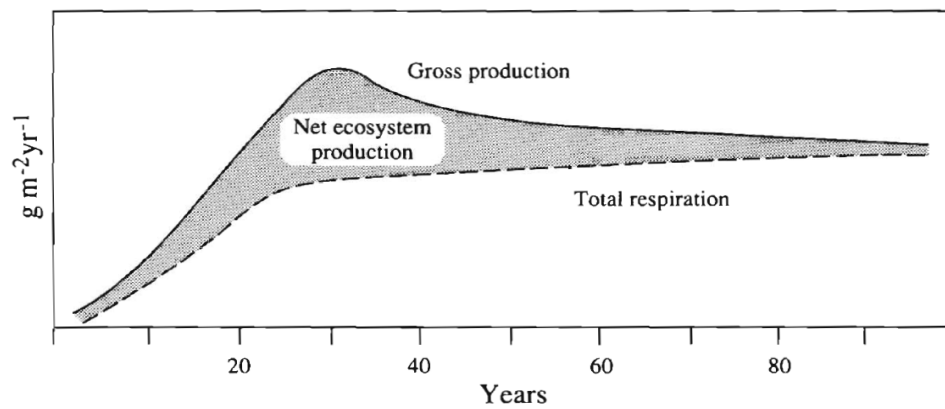


Figure 5.13 Generalized trends in primary production and respiration during ecosystem development. Modified from Odum (1969).

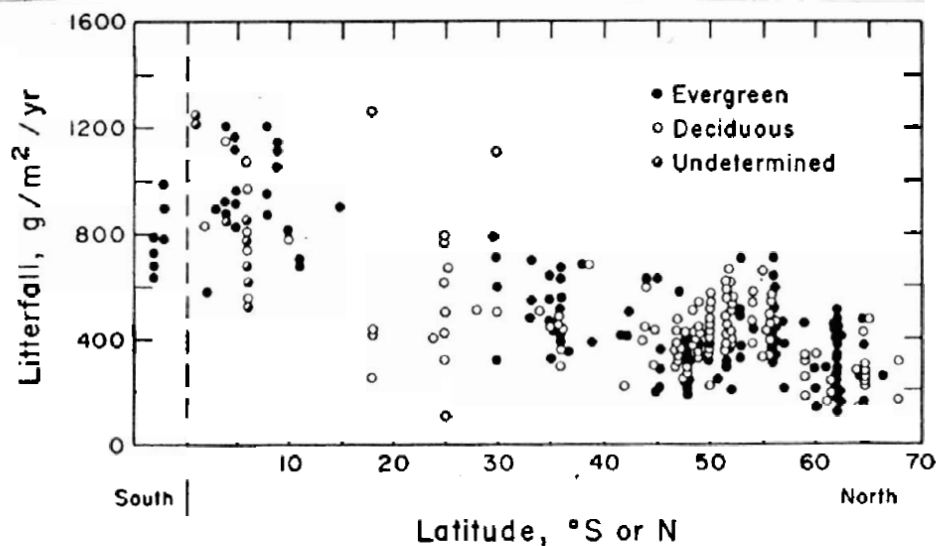


Fig. 8.1. Annual litterfall in forest ecosystems of the world (From Van Cleve *et al.*, 1983, with permission from *Can. J. For. Res.* 13, 747-766. *Warning + Schlesinger 1985*)

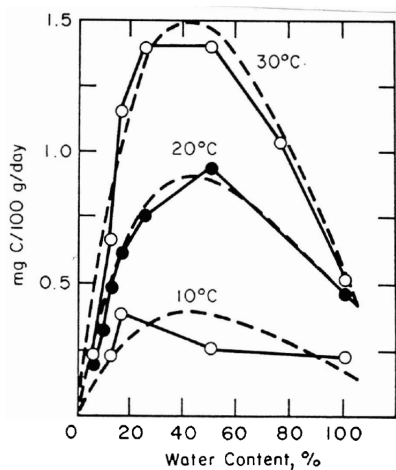


Fig. 8.7. Release of C as CO₂ due to the activity of soil microorganisms at varying temperature and soil moisture content. (From Ino and Monsi, 1969.) *Warning + Schlesinger 1985*

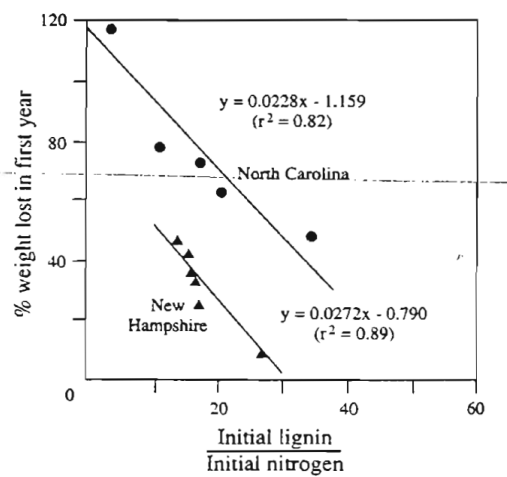


Figure 6.7 Decomposition of leaf litter as a function of the lignin/nitrogen ratio in fresh litterfall of various forest species in New Hampshire and North Carolina. From Melillo *et al.* (1982).

Biome	World area (10 ⁶ km ²)	Mean soil profile carbon (kgC/m ²)		Total soil carbon pool (10 ¹⁵ gC) 0-300 cm
		0-100 cm	0-300 cm	
Tropical forests				
Deciduous	7.5	15.8	29.1	218
Evergreen	17.0	18.6	27.9	474
Temperate forests				
Deciduous	7	17.4	22.8	160
Evergreen	5	14.5	20.4	102
Boreal forests	12	9.3	12.5	150
Mediterranean shrublands	8.5	8.9	14.6	124
Tropical savannas/grasslands	15	13.2	23.0	345
Temperate grasslands	9	11.7	19.1	172
Deserts	18	6.2	11.5	208*
Arctic tundra	8	14.2	18.0	144
Crops	14	11.2	17.7	248
Extreme desert, rock and ice	15.5			
Total	136.5			2344

Ecosystem Type	World Area (ha × 10 ⁸)	Total World Litter (mt C × 10 ⁹)
Tropical forest	24.5	3.6
Temperate forest	12	14.5
Boreal forest	12	24.0
Woodland and shrubland	8.5	2.4
Tropical savanna	15	1.5
Temperate grassland	9	1.8
Tundra and alpine	8	4.0
Desert scrub	18	0.2
Extreme desert, rock and ice	24	0.02
Cultivated	14	0.7
Swamp and marsh	2	2.5
Totals	147	55.2

*From Schlesinger (1977).

